

Robustness of negative low-field magnetoconductance in ultrathin topological insulator filmsXuefan Niu ^{1,2}, Yuxin Liu,^{1,2} Jing Teng ^{1,2,*} and Yongqing Li ^{1,2,3,†}¹*Beijing National Laboratory of Condensed Matter Physics, Institute of Physics, Chinese Academy of Sciences, Beijing 100190, China*²*School of Physical Sciences, University of Chinese Academy of Sciences, Beijing 100049, China*³*Songshan Lake Materials Laboratory, Dongguan, Guangdong 523808, China*

(Received 25 November 2022; accepted 22 February 2023; published 6 March 2023)

In the ultrathin films of three-dimensional topological insulators (TIs), modification of the Berry phase caused by surface hybridization was predicted to allow for a crossover between weak antilocalization (WAL) and weak localization (WL). Here we report on a systematic study of the magnetotransport properties of $(\text{Bi}_{1-x}\text{Sb}_x)_2\text{Te}_3$ (BST) thin films with well-controlled thickness, doping level, and chemical potential. We found that the sign of magnetoconductance in perpendicular magnetic field remains negative in all circumstances, suggesting absence of global WL in the ultrathin BST films. This is attributed to long-range disorder, as well as conductance corrections by quantum interference and electron-electron interaction. Our work shows that the electron transport in ultrathin TIs is distinctively different from the WAL regime in the systems with symplectic symmetry, and the WL or weak insulator regime associated with the orthogonal symmetry class.

DOI: [10.1103/PhysRevB.107.115112](https://doi.org/10.1103/PhysRevB.107.115112)**I. INTRODUCTION**

Negative magnetoresistance caused by the weak localization (WL) is one of the most widely studied electron transport phenomena in low-dimensional systems [1–3]. For an electron system with negligible spin-orbit coupling, the WL effect can be attributed to *constructive* quantum interferences between time-reversed loops in self-crossed electron trajectories. When a perpendicular magnetic field is applied, the randomness in the Aharonov-Bohm phases of various loops suppresses the quantum interference and thus leads to positive magnetoconductance (MC). As the strength of spin-orbit coupling (SOC) increases, a crossover to weak antilocalization (WAL) takes place and is manifested as negative MCs in low magnetic fields. Such a WL-WAL crossover can be described by the seminal Hikami-Larkin-Nagaoka (HLN) equation [4]. From a more general point of view, this crossover is a consequence of underlying symmetry change from orthogonal to symplectic, and thus should not be restricted to the systems with tunable SOC strengths. One example is graphene, in which the π Berry phase due to the pseudospin-momentum locking could in principle give rise to a canonical WAL effect [5,6]. However, only positive MCs were observed in the early transport measurements of graphene, due to the presence of strong intervalley or chirality-breaking scatterings [7–10]. Tikhonenko *et al.* later showed that a crossover from the WL to the WAL could be induced by carefully tuning electron's dephasing rate relative to the intervalley and chirality-breaking scattering rates [11].

The surface states of three-dimensional topological insulators (3D TIs, referred to as TIs below for brevity), represent another important type of two-dimensional (2D)

Dirac fermion systems, in which the π Berry phase originates from locking of the momentum to real electron spin [12,13]. Similar to graphene, TI surface states are expected to exhibit many interesting transport properties, such as half-integer quantum Hall effect [14,15], suppression of backscattering [16], and crossover between the WL and WAL [17]. Interestingly, negative MCs due to the WAL can be easily observed in TIs, either in the samples with dominating surface transport [18–21], or in those with significant bulk conductivity [22–24]. This is in stark contrast with graphene, in which observation of the WAL is possible in a very limited temperature range [11]. For TIs, nevertheless, an experimental confirmation of the crossover to the WL remains as a daunting task, despite that several different approaches have been considered, including surface hybridization [17], magnetic doping [17,25,26], and magnetic proximity effect [27–29].

In the past decade, considerable efforts have been devoted to investigate electron properties of ultrathin TIs [30–36]. The hybridization between the surface states of the top and bottom surface can not only open an energy gap whose size increases with decreasing film thickness [37–39], but also modify the symmetry of the electron system because of the opposite spin helicities possessed by these two surfaces. A crossover from the WAL to the WL is hence expected to occur. This crossover may also be interpreted with the modified Berry phase of surface Dirac fermions [17], which become massive in ultrathin TIs [37–39]. When the Fermi energy E_F decreases from large values toward the edge of hybridization gap, the Berry phase varies from π to 0, and the sign of MC is anticipated to flip from negative to positive [17]. On the experimental side, spectroscopic experiments have provided evidence for the hybridization gap in the TI films with thicknesses less than 6 nm [40–43]. A spin-resolved photoemission experiment revealed a hedgehoglike spin texture in the surface states of ultrathin TI films, further supporting the massive Dirac fermion model [44]. In the transport measurements, however,

*jteng@iphy.ac.cn

†yqli@iphy.ac.cn

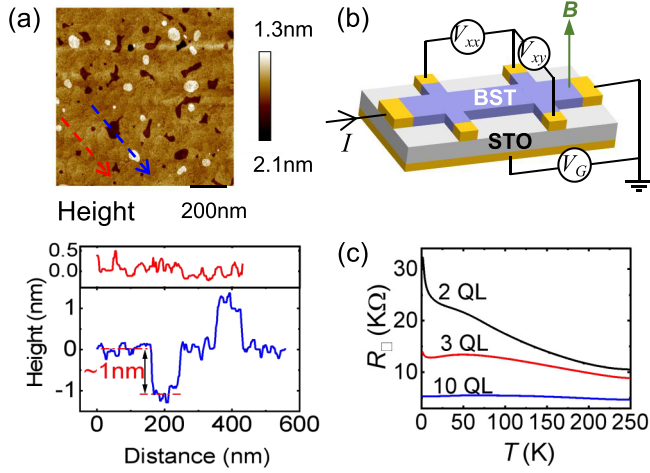


FIG. 1. Characterization of $(\text{Bi, Sb})_2\text{Te}_3$ films and Hall bar devices. (a) Atomic force microscopy image of a 3 QL (nominal) $(\text{Bi, Sb})_2\text{Te}_3$ film grown on STO substrate, with the line profile showing the terrace heights on the TI surface (blue arrow line) and the STO substrate (red arrow line). (b) Schematic sketch of Hall bar device equipped with a back gate. The magnetic field is aligned along \bar{z} direction (or perpendicular to the sample plane). (c) Temperature dependencies of sheet resistance R_{\square} of 2 QL, 3 QL, and 10 QL $(\text{Bi, Sb})_2\text{Te}_3$ films (samples A–C).

positive low-field MCs manifesting the WAL-WL crossover have rarely been reported for ultrathin TIs despite a lot of experimental efforts [30–36]. In most cases, only negative MCs were observed, albeit at much reduced magnitudes. It remains to be understood why the crossover to the WL is so difficult to realize in ultrathin TIs.

In this work we address this puzzling issue by carrying out a detailed study of $(\text{Bi}_{1-x}\text{Sb}_x)_2\text{Te}_3$ (BST) ($x = 0-1$) films with well-protected top surface and well-controlled chemical potential. By carefully varying the film thickness, the hybridization gap is changed from virtually zero up to about 0.1–0.2 eV. The chemical potential can be tuned *across* the hybridization gap with a back gate. Although the magnitude of low-field MC can be reduced significantly, its sign remains negative, regardless of the gate voltage, film thickness, and temperature. The robustness of negative MC is explained by taking account of disorder-induced long-range electrostatic potential fluctuations and suppression of the WL effect by high-order quantum corrections. Implications of these results are also discussed.

II. EXPERIMENTAL METHODS

The BST films used in this work were grown on $\text{SrTiO}_3(111)$ (STO) substrates with molecular beam epitaxy (MBE) [45]. The growth condition was optimized to obtain the smooth surface morphology illustrated in Fig. 1(a), in which the major step height is nearly 1 nm, corresponding to 1 quintuple layer (QL) of BST. The Bi/Sb composition ratio was adjusted to make the Fermi level close to the charge neutral point (CNP) at zero gate voltage. The ultrathin BST films, which refer to the films thinner than 6 QLs in this work, were encapsulated with a Te layer to avoid surface

degradation, before being taken out of the MBE chamber and patterned into the Hall bars schematically depicted in Fig. 1(b) (see Hall bar image in Fig. S3 [46]). The transport measurements were carried out in a ^4He vapor flow cryostat and a ^3He system using lock-in amplifiers operated at low frequencies. The excitation current was set in a range of 10–100 nA in order to prevent heating or other spurious effects. The magnetic field was applied perpendicular to the TI films with a superconducting magnet throughout this work. The data presented below were collected from BST samples with thicknesses from 2 QLs to 10 QLs [46].

III. EXPERIMENTAL RESULTS

R-T characteristics. Figure 1(c) shows the temperature dependencies of longitudinal resistance per square, denoted as R_{\square} , for three BST films (samples A–C). Sample A is 10-QL thick, so the hybridization between the top and bottom surface states is negligible [47]. For this sample, R_{\square} varies slightly with temperature and has a maximum value of about 5 k Ω . In contrast, the two ultrathin samples (samples B and C, 3 and 2 QLs thick, respectively) have much larger R_{\square} values and exhibit stronger temperature dependencies. For instance, R_{\square} of sample C exceeds 20 and 30 k Ω at $T = 50$ and 2 K, respectively. The overall R - T characteristics of these samples are consistent with previously reported works [34,45], in which the surface hybridization gap is invoked to account for the greatly enhanced R_{\square} in ultrathin BST films in comparison with thicker samples with gapless surface states.

Gate-voltage dependencies. Figure 2(a) depicts the gate-voltage dependencies of R_{\square} and Hall coefficient R_H for samples A, B, and C. Throughout this work, R_H is defined as dR_{yx}/dB , so it is negative (positive) for the transport dominated by electrons (holes). The Hall resistance curves at various gate voltages are linear in magnetic fields up to at least 2 T (see [46] Fig. S4). However, the linearity does not necessarily mean only one type of charge carriers contributing to the transport. If there exist two types of carriers, and their mobilities are sufficiently low so that $\mu_i B \ll 1$ ($i = 1, 2$), the Hall resistance can be simplified into linear form:

$$R_{yx}(B) = \frac{1}{e} \frac{(n_1 \mu_1^2 + n_2 \mu_2^2)}{(|n_1| \mu_1 + |n_2| \mu_2)^2} B + O(B^3) \simeq R_H B, \quad (1)$$

where $|n_1|$ and $|n_2|$ are the carrier densities of carrier types 1 and 2, respectively, and μ_1 and μ_2 are the corresponding mobilities. Here, n_1 and n_2 take negative values for electrons and positive values for holes. Consequently, the magnitude of R_H can be reduced significantly when both electrons and holes are present (i.e., the transport is in the ambipolar regime). It follows that the nominal carrier density, given by $n_H = 1/|eR_H|$, could be much higher than the real density of either type of carriers. For a gate-tuned TI thin film, the ambipolar transport is associated with, but not limited to, the region between the maximum and minimum of R_H [the gray area in Fig. 2(a)].

Figure 2(b) shows that the $|R_H|$ values at large negative gate voltages are much smaller than their counterparts at $V_G > 0$ for samples A–C. Such a particle-hole asymmetry is most pronounced for sample A, in which R_H takes a minimum value of about $-300 \Omega/\text{T}$ at $V_G \approx 30$ V, contrasting with a maximum of about $30 \Omega/\text{T}$ at $V_G \approx -120$ V. Were there only

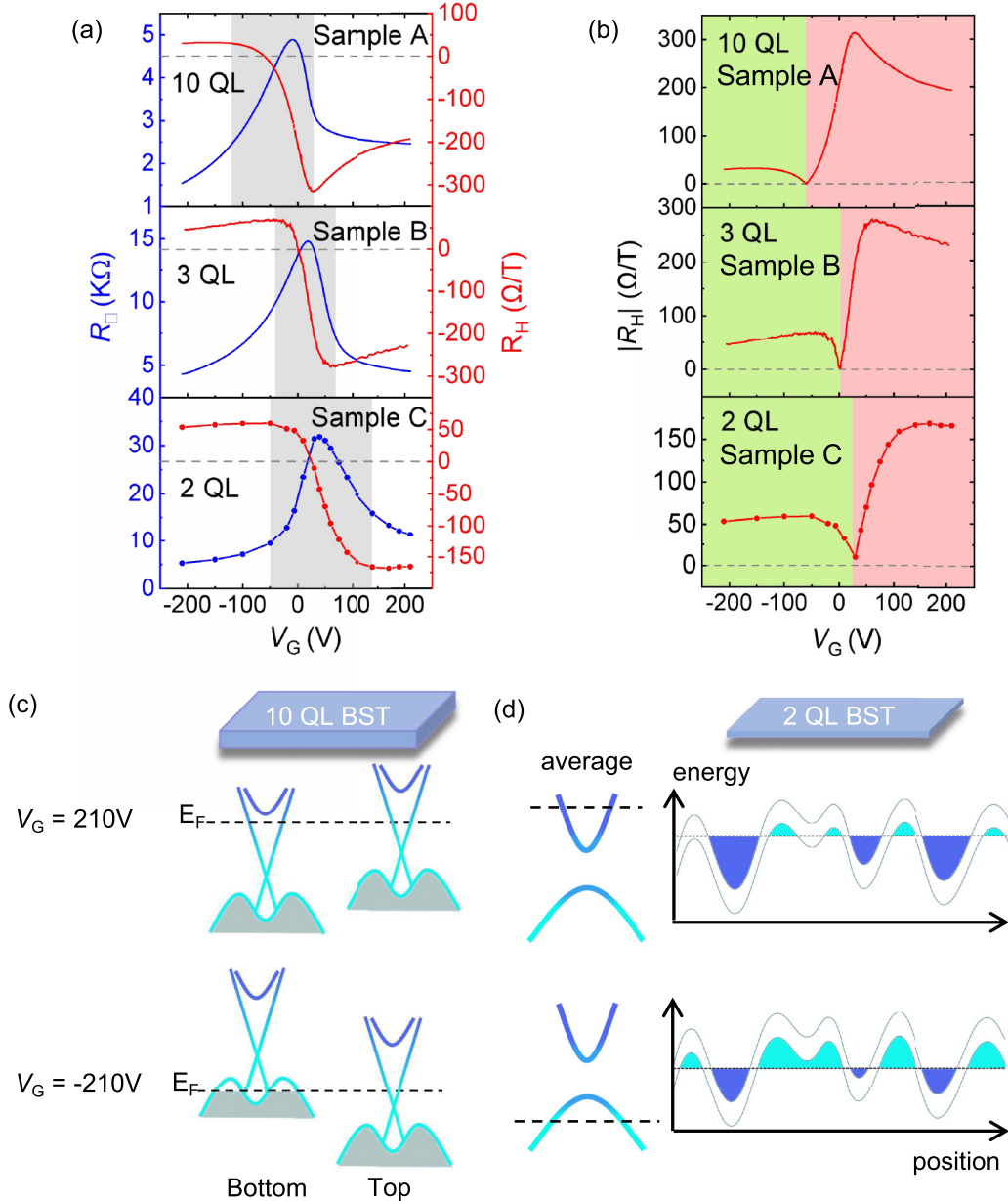


FIG. 2. Gate-voltage dependencies of sheet resistance and Hall coefficient. (a) R_{\square} and R_H of samples A–C plotted as a function of V_G . The gray area denotes the region between the maximum and minimum of R_H , in which the transport is ambipolar. Measurements were conducted at $T = 0.3$ K for sample A, and 1.7 K for samples B and C. (b) Asymmetry in $|R_H|$ for samples A–C. (c) Schematic band diagrams of samples A (10-QL film), in which the surface states are gapless, at $V_G = \pm 210$ V. At -210 V, E_F of the bottom surface drops below the top of bulk valence band, while E_F of the top surface lies in the upper branch of surface state band. At 210 V, E_F of the bottom surface is lifted up to the surface state. (d) Illustration of the gating and the long-range disorder effects for the ultrathin TI film (sample C).

holes participating in the transport, the small R_H values at $V_G < -100$ V would correspond to unrealistically high hole densities ($2 \times 10^{13} \text{ cm}^{-2}$ or higher). The strong asymmetry in R_H is not uncommon in the BST thin films grown with MBE [45,48,49]. It can be attributed to a large difference in the chemical potential between the top and bottom surfaces. The corresponding band diagram of 10-QL film is schematically depicted in Fig. 2(c). At $V_G \geq 0$, the Fermi level lies above the Dirac point for both surfaces; whereas at large negative gate voltages the bottom and top surfaces becomes p type and n type, respectively, owing to the single-sided gating

and the screening effect of the bottom surface. Existence of the electrostatic potential gradient is further supported by a large offset between the R_{\square} maximum and the zero- R_H point, which are located at $V_G = -10$ and -60 V, respectively.

Although the particle-hole asymmetry (much smaller $|R_H|$ values at negative gate voltages than that at positive gate voltages [Fig. 2(b)]) is observed for BST films of all thicknesses, the underlying mechanism is different for the 10-QL sample from the ultrathin samples. In samples B and C, the surface hybridization generates a sizable mass gap (about 0.05–0.2 eV) [40–43], so the electron wave functions of

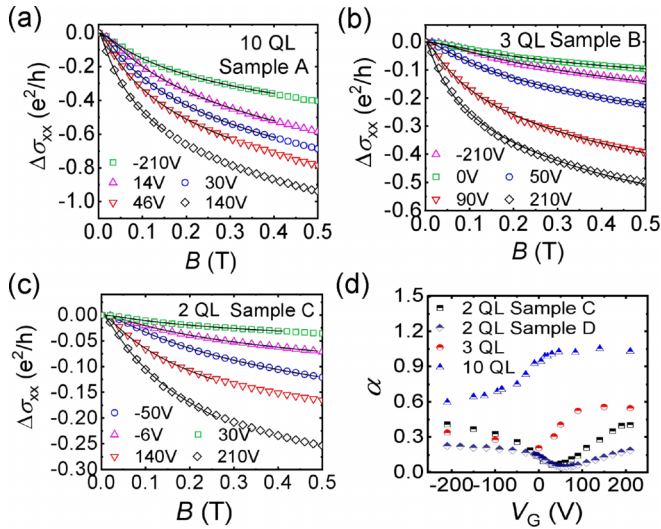


FIG. 3. Magnetoconductances (MCs) of BST films with various thicknesses. (a)–(c) Low-field MCs of samples A (10 QL), B (3 QL), and C (2 QL) at various gate voltages. The experimental data are plotted with open symbols and the solid lines are the best fits to Eq. (2). (d) Gate-voltage dependence of prefactor α obtained from the HLN fits of the MC curves. The transport measurements were conducted at $T = 1.7$ K for 2-QL and 3-QL films, and 0.3 K for the 10-QL film (sample A).

the two surfaces become strongly hybridized. The single-sided gating can thus influence both surfaces with comparable strengths. This is consistent with the gate-voltage dependencies of dual-gated TI flakes with hybridization gap, in which R_{\square} is quite insensitive to the electrical displacement field, but varies strongly with the total sheet carrier density [50]. In comparison with sample A, sample B has a more pronounced R_H maximum (70 Ω/T at $V_G = -40$ V) and smaller asymmetry in $|R_H|$. The degree of asymmetry may be characterized by the ratio between the magnitudes of R_H maximum and minimum, $|R_{H,\min}|/|R_{H,\max}|$. For sample B, it is about 4, slightly larger than $|R_{H,\min}|/|R_{H,\max}| \approx 3$ for sample C. Both ratios are considerably smaller than $|R_{H,\min}|/|R_{H,\max}| \approx 10$ for sample A. We attribute the asymmetry in $|R_H|$ to long-range disorder and an asymmetry in the band structure of BST (i.e., the Dirac point in proximity to the bulk valence band, instead of the conduction band) [47,51]. The former leads to the formation of electron and hole puddles in the ambipolar regime [52,53], whereas the latter enables the electron puddles to persist even when the bulk valence band gets populated. Due to the high density of states in the bulk valence band, the Fermi level does not change much at the large negative gate voltages, leading to the coexistence of electron puddles and hole carriers and hence large reductions in $|R_H|$. The disorder effect is schematically illustrated in Fig. 2(d), and will be further discussed in Sec. IV.

Magnetoconductivity. Figure 3 displays the main experimental results of this work, namely, the low-field MCs being negative for all circumstances. This phenomenon is not surprising for sample A, in which the WAL effect of the gapless surface states is responsible for the cusp-shaped negative MC [Fig. 3(a)]. Similar results have been obtained frequently in previous experiments [54]. The MC, defined as $\Delta\sigma(B) =$

$\sigma(B) - \sigma(0)$, follows the HLN equation simplified for the strong SOC limit and low magnetic fields:

$$\Delta\sigma(B) \cong -\alpha \frac{e^2}{2\pi^2\hbar} \left[\Psi\left(\frac{1}{2} + \frac{B_\phi}{B}\right) - \ln\left(\frac{B_\phi}{B}\right) \right], \quad (2)$$

where α is a prefactor, $\Psi(x)$ is the digamma function, B_ϕ is the dephasing field. For an ideal case of the WAL, α takes a value of $n/2$, with n being the number of independent, equivalent transport channels. In practice, the top and bottom surfaces can be inequivalent, and they could couple to each other via surface hybridization or surface-bulk coupling. The MC data can nevertheless be fitted to Eq. (2) quite well, if prefactor α is treated as a free-fitting parameter. The obtained α value often deviates substantially from $n/2$. In this case, the α value also provides valuable information to gain insight into the electronic states in TIs. For instance, α of sample A varies from slightly over 1 at $V_G > 20$ V to about 0.6 at $V_G = -210$ V, suggesting a crossover from two independent channels of nearly equivalence to a bilayer system of strong asymmetry [21,22,34]. In the latter, the dephasing fields of the top and bottom surfaces differ from each other significantly since the bottom-gating exerts a stronger influence on the bottom surface than the top surface.

For the two ultrathin BST samples [Figs. 3(b) and 3(c)], the overall characteristics of the MC curves seem to resemble those of the 10-QL sample at the first glance. The extracted α values, however, exhibit drastically different behaviors for these two types of samples. As depicted in Fig. 3(d), prefactor α of sample A has a nearly monotonic gate-voltage dependence and never drops below $\frac{1}{2}$. In contrast, for samples B and C, α varies nonmonotonically with the gate voltage, with a minimum appearing near the CNP. Figure 3(d) also shows that the α values of the ultrathin samples are much reduced in comparison with those of sample A, with a minimum value as low as 0.05 for the 2-QL films (samples C and D, see [46] for the transport properties of sample D). It is worth noting that α remains positive at any gate voltage for all BST samples studied in this work.

IV. DISCUSSION

Comparison with previous results. Prior to this work, several groups, including some of us, studied the magneto-transport properties of ultrathin TI films [30–36]. For the samples gated electrically, the maximum in the sheet resistance per square $R_{\square,\max}$ could usually be obtained. It was found that $R_{\square,\max}$ is sensitive to the film thickness and considerably larger than its 3D TI (gapless) counterparts [34]. The $R_{\square,\max}$ value can work as a convenient measure of the surface hybridization effect. However, $R_{\square,\max}$ is also susceptible to sample preparation and storage conditions. For instance, Nandi *et al.* observed that $R_{\square,\max}$ of a 4-QL BST film could spread from about 6 to 28 k Ω . We found that insufficient protection of the top surface could make $R_{\square,\max}$ of a 2-QL TI film exceeding 100 k Ω or even 1 M Ω . In the latter case, the transport may enter the Anderson localization regime, which is the focus of Ref. [34]. In this work, we stay away from the strong localization by *in situ* encapsulating the BST films with Te layers, and taking additional measures to prevent the surface from post-growth degradation (see Sec. II). The

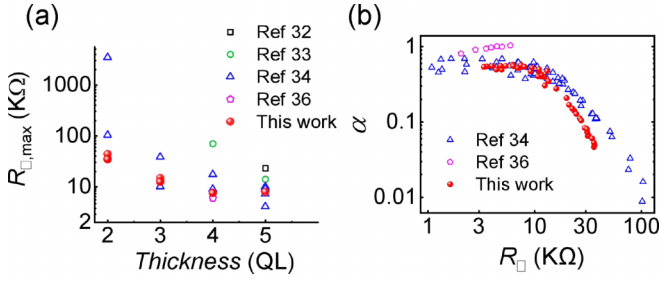


FIG. 4. Correlation between prefactor α and sheet resistance in ultrathin TI films. (a) $R_{\square, \max}$ vs film thickness for various TI films, including the results of this study (red circles) and previous reports [32–34,36]. (b) Dependence of the corresponding prefactor α on R_{\square} .

improvement in the quality of BST samples is manifested in two aspects: (1) the $R_{\square, \max}$ values of 2-QL samples are only 32–36 $k\Omega$, (2) the sample-to-sample variation in $R_{\square, \max}$ is much reduced for the ultrathin films of certain thickness, as shown in Fig. 4(a).

In most of the previous studies [30–32,34,36], the low field MC is negative for $R_{\square} < 100$ $k\Omega$. Table I gives the minimum α values reported in the literature, along with those of samples C and D. The α values are much reduced in comparison with their 3D TI (gapless) counterparts, but remain positive [55]. In Ref. [34], the decrease in α is correlated with the increase in R_{\square} . Figure 4(b) shows that it is consistent with the data from this work.

Inconsistency between the MC data and the LSS formula. In the previous studies of ultrathin TIs, interpretations of the MC data often relied on the theory of Lu, Shi, and Shen (LSS) [17], who extended the HLN equation by taking account of the modified Berry phase. In a 2D massive Dirac fermion system, the Berry phase is a function of the ratio between the Fermi energy E_F and the mass gap Δ : $\varphi_B = \pi(1 - \frac{\Delta}{2E_F})$. As the Fermi energy is lowered from the $E_F \gg \Delta/2$ limit toward the gap edge ($E_F \sim \Delta/2$), φ_B varies from π to 0, leading to the WAL-WL crossover. This prediction has inspired a lot of experimental investigations on the massive surface states in

TABLE I. Summary of previous MC measurements of ultrathin TI films. Results for $R_{\square} > 100$ $k\Omega$ are not included.

Material	Thickness (QLs)	$R_{\square, \max}$ ($k\Omega$)	T (K)	α_{\min}	Reference
Bi_2Se_3	2,3,5	^a	1.6	~ 0	[30]
Bi_2Se_3	2,3,4	^a	1.5	~ 0.4	[31]
Bi_2Se_3	5	23	2	0.1	[32]
$(\text{Bi}, \text{Sb})_2\text{Te}_3$	4, 5	70	0.3	< 0	[33]
Bi_2Se_3	3, 5	37	1.6	0.1	[34]
$(\text{Bi}, \text{Sb})_2\text{Te}_3$	2,3	100	1.6	0.01	[35]
$(\text{Bi}, \text{Sb})_2\text{Te}_3$	4	~ 28	0.03	^b	[36]
$(\text{Bi}, \text{Sb})_2\text{Te}_3$	4	~ 6	0.03	0.8	[36]
$(\text{Bi}, \text{Sb})_2\text{Te}_3$	2	32	1.7	0.06	This work ^c
$(\text{Bi}, \text{Sb})_2\text{Te}_3$	2	36	1.7	0.05	This work ^d

^aThis sample was not gated.

^bNo MC data are available for this device.

^cData are taken from device C.

^dData are taken from device D.

TIs, including nonmagnetic and magnetic systems [25–36]. In the LSS theory, the MC is written as the sum of a WAL-like term and a WL-like term:

$$\Delta\sigma(B) \cong -\sum_{i=1,2} \alpha_i \frac{e^2}{2\pi^2\hbar} \left[\Psi\left(\frac{1}{2} + \frac{B_{\varphi i}}{B}\right) - \ln\left(\frac{B_{\varphi i}}{B}\right) \right], \quad (3)$$

where α_i is the prefactor of term i ($i = 1, 2$), and $B_{\varphi i} = \frac{\hbar}{4De}(\frac{1}{l_i^2} + \frac{1}{l_i^2})$, with l_i being a characteristic length taking the surface hybridization effect into account. The signs of α_1 and α_2 are opposite to each other, and their relative weight $|\alpha_1/\alpha_2|$ is a function of the Berry phase and can vary from 0 to ∞ . Therefore, the MC can be negative, positive, or completely vanished at low magnetic fields.

The essence of the LSS theory is the modification of the first-order quantum interference effect by the Berry phase that varies with the ratio E_F/Δ in the weakly disordered ($k_F l \gg 1$) regime. The reduced α values obtained previously for ultrathin TIs have mostly been attributed to the crossover between the WAL and WL within the LSS framework [30,32,33]. However, such an interpretation is inconsistent with the following two experimental facts: (1) MC remains negative when the Fermi energy is tuned from $E_F \gg \frac{\Delta}{2}$ to lower values and across the hybridization gap, whereas the LSS theory predicts existence of positive MC near the gap edge; (2) in case of greatly suppressed prefactor α , R_{\square} is usually larger than 10 $k\Omega$ so that the transport is not in the weakly disordered regime, which is a prerequisite for the well-defined WL effect. As we argue below, the discrepancies between the theory and experiment originate from negligence of long-range disorder as well as the second-order quantum corrections in the LSS theory.

Long-range disorder in TIs. During the past decade, remarkable progress has been made in understanding the disorder effects in TIs. First, long-range Coulomb disorder was found necessary to explain the charge puddles observed in TI surface states [36], much reduced or vanishing thermal activation gap in compensated TI materials [36,56], and mesoscopic scale photocurrent patterns [57] and linear magnetoresistance [36] in BST thin films. One source of the long-range disorder originates from correlated Coulomb potential produced by the charged defects in compensated TIs [56]. For the ultrathin BST films grown on STO, additional sources of long-range disorder include thickness fluctuations on the level of ± 1 QL, and subnanometer high terraces on the STO surface [Fig. 1(a)]. These types of disorder can induce chemical potential fluctuations with length scales of the order 10 nm to 1 μm . In the LSS theory, however, the chemical potential is assumed to be spatially homogeneous since only the short-range disorder is considered. Second, in both the HLN and LSS equations, only the first-order interference effect is included. This is justified for the weak disorder regime ($k_F l \gg 1$). This condition is, however, not always fulfilled in TIs. Higher-order quantum effects, including the second-loop interference and electron-electron interaction (EEI), were recently found indispensable to account for the enhanced MCs in $(\text{Bi}, \text{Sb})_2(\text{Te}, \text{Se})_3$ (BSTS) flakes in the intermediate disorder regime, in which $k_F l \gg 1$ no longer holds, but $k_F l > 1$ is satisfied [58]. It is also worth noting that Minkov *et al.* discovered long ago that for the intermediate conductance,

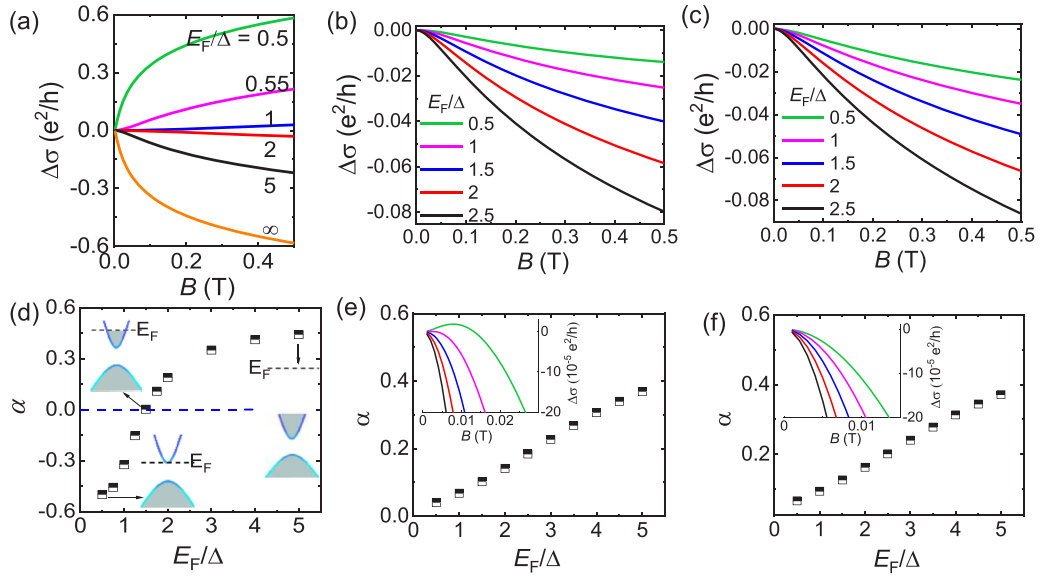


FIG. 5. Numerically calculated MCs for ultrathin TIs. (a) MC calculated with Eq. (3) with $l_\phi = 300$ nm. Neither long-range disorder nor second-order quantum correction effect is included. (b) MCs calculated with long-range disorder effect considered. Chemical potential fluctuations are assumed to have a Gaussian distribution with a standard deviation of 2Δ . (c) MCs calculated with the incorporation of both long-range disorder effect and second-order corrections. A suppression factor 0.01 is applied for the case of Fermi energies lower than Δ ($E_F < \Delta$). (d)–(f) Prefactor α as a function of E_F/Δ for the calculated MC curves shown in (a), (b), and (c) respectively. The insets in (d) and (f) are zoom in of (c) and (d) near zero magnetic field, respectively [also shown in Figs. S8(b) and S8(c) for details [46]].

the WL effect can be suppressed significantly in conventional semiconductor 2D systems [59]. In both cases, the low-field MC data can still be fitted well with Eq. (2). The higher-order quantum corrections, mainly of the order of $1/g$, are manifested in increased or reduced magnitude of prefactor α . Given that the $k_F l$ values can be less than 2 in the ultrathin BST films, we expect similar higher-order quantum corrections to be relevant. As detailed below, this is a key ingredient to explain the robustness of negative MC in the ultrathin TIs.

Strength of long-range disorder. As discussed in Sec. II, the large asymmetry in the gate-voltage dependence of $|R_H|$ suggests the existence of strong disorder in the ultrathin BST films. This leads to the formation of electron puddles even in presence of a high density of holes. The peak-to-peak spatial fluctuations in the chemical potential are expected to be greater than the hybridization gap, which is about 0.1–0.2 eV for the 2-QL BST samples [40–43]. In addition, the hybridization gap is spatially inhomogeneous due to the fluctuations in the film thickness. For instance, it may drop to about 0.05 eV in the 3-QL thick regions [see Fig. 1(a)]. One way to estimate the strength of long-range disorder is to make use of the maximum value of Hall coefficient $|R_H|$. For the gapless TIs, we generally use the linear dispersion law and the magnitude of carrier density fluctuations Δn to estimate the average magnitude of fluctuations ($\Delta\mu$) in local chemical potential $\mu(r)$, that is, $\Delta\mu = 2\hbar v_F \sqrt{2\pi \Delta n}$ where v_F is the Fermi velocity. Δn can be evaluated from the maximum $|R_H|$ value. This has proven to be a valid approach in graphene and BSTS flakes. In high-quality graphene with carrier mobility of nearly 10^6 cm²/V s, the maximum $|R_H|$ is over 200 k Ω /T [60]. In dual-gated BSTS microflakes, the mobility is typically 10^3 – 10^4 cm²/V s and the maximum

$|R_H|$ is about 3.5 k Ω /T [14]. Using linear dispersion and Fermi velocity of about 5×10^5 m/s, one could estimate the average magnitude of chemical potential fluctuations to be about 25 meV in the microflakes exfoliated from BSTS single crystals. For the 10-QL sample grown on STO, the maximum $|R_H|$ is about 0.3 k Ω /T. A similar analysis yields a disorder strength of about 85 meV, roughly 3–4 times that of the BSTS flakes. The disorder strength is expected to be stronger in ultrathin samples because the entire sample is susceptible to the defects at the bottom interface and the top surface, as a consequence of the surface hybridization. For an ultrathin TI with a sizable hybridization gap (i.e., <4 QLs BST film), stronger disorder broadening is expected to reach the same value of the R_{yx} maximum or minimum, in comparison with the gapless counterpart. Since the conductivity at the R_{xx} maximum is still substantial even for the 2-QL sample, the disorder broadening is larger than the gap size. Because the transport is not in the well-defined diffusive transport regime, it is extremely difficult to quantitatively evaluate the width of disorder broadening based on the values of R_{yx} extrema, which are strongly asymmetric due to the particle-hole asymmetry. The numerical simulation results presented in Sec. IV provide a *posteriori* justification of the above speculation.

Calculation of the MC. We have carried out numerical calculations of the MC for the ultrathin BST films. Figure 5(a) shows the results from the original LSS equation, with neither long-range disorder nor second-order quantum corrections considered. As the Fermi level approaches the hybridization gap from above, the MC changes from negative to positive at $E_F/\Delta \approx 1.5$. At the gap edge ($E_F/\Delta = 0.5$), prefactor α drops to -0.5 [Fig. 5(d)], suggesting a well-defined WL behavior. Figure 5(b) shows the results with the long-range

disorder effect included. Here, the fluctuations in the chemical potential are assumed to have a Gaussian distribution with a standard deviation of $\delta = 2\Delta$. The LSS equation was used to evaluate the local MC for each possible value of chemical potential μ , and the contributions of all possible μ values are then added up with proper weights. As depicted in Fig. 5(b), the calculated MC curves can reproduce the main features of the experiment. The α values, obtained from the HLN fits of the numerically generated MC curves [see Fig. 5(e)], remain positive for all cases. As the average Fermi energy (E_F) approaches the gap edge, α drops toward zero, also consistent with the data shown in Fig. 4(b). A closeup examination of the MC data, however, reveals that the low-field MC can be positive for small $\langle E_F \rangle / \Delta$ values [inset of Fig. 5(e), as well as Fig. S8(a) [46]]. This may be regarded as reminiscent of the crossover to WL, but has not yet been observed in our experiment. Such a discrepancy is not surprising. As discussed above, the small $k_F l$ values in ultrathin TI films make the second-order quantum corrections to MC no longer negligible, which enhances the negative MC due to the WAL [58] and suppresses the positive MC related to the WL [59]. For the case of WL, the transport may enter the so-called weak insulator (WI) regime [59], in which the conductance can be greatly reduced and the magnitude of α could approach zero, if $k_F l < 3$. In the ultrathin TI films, strong long-range fluctuations make the local E_F / Δ values spread in a large range, separating the surface states into WAL- and WL(WI)-like regions. The former is expected to have much higher conductivity than the latter, so the current density distributes inhomogeneously. It is also noteworthy that the $k_F l$ value evaluated from R_{\square} is a spatially averaged quantity. The local $k_F l$ values for the WL(WI) regions should be even smaller. This, along with the suppressed α for the WI-like regions, makes the total MC dominated by the WAL-like regions. Figures 5(c) and 5(f) depict the calculated results with a suppression factor 0.01 applied to the MCs for the local Fermi energies lower than Δ [46]. This treatment does not change the overall shape of the MC curves or the Δ values. The main improvement is that the MC remains negative in the low magnetic field region [inset of Fig. 5(f), as well as Fig. S8(b) [46]]. We also performed calculations with different levels of energy fluctuations [$\delta = 0.5\Delta$ to 2.5Δ , see [46], Fig. S8(c)]. We found that the MC curves obtained for $\delta = 2\Delta$ are in best agreement with the experiment, further supporting our estimation of the disorder strength and the hybridization gap for the 2-QL BST films.

Comparison with other types of electron systems. Finally, we would like to point out that the study of the MC in ultrathin TI films enables us to reveal a unique transport regime that is distinctively different from the WAL of the symplectic symmetry class and the WL of the orthogonal class. It is manifested as a special range of prefactor (i.e., $\alpha \sim 0-0.5$) with α monotonically decreasing with increasing $1/g$. In contrast, for the WAL effect seen in thicker (truly 3D) TIs with two equivalent surfaces, α becomes larger than 1 due to the enhancements by the second-order quantum interference and EEI effects, both of which are of the order $1/g$ [58]; for the WL effect observed in conventional semiconductor 2D systems, α has an opposite sign and its magnitude could be reduced by the higher-order quantum corrections. If the

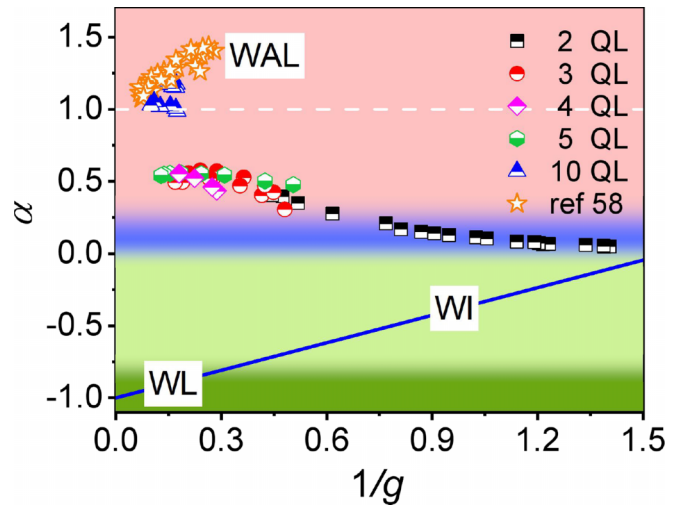


FIG. 6. Prefactor α plotted as a function of $1/g$ for various transport regimes. The data for BSTS flakes with gapless surface states, taken from Ref. [58], is shown as an example for symplectic electron systems. The solid line follows equation $\alpha = -1 + \frac{2}{\pi g}$, which a conventional 2D system with orthogonal symmetry would follow [59]. The data extracted from BST films with various thicknesses in our experiments are drawn in symbols.

disorder effect is weak ($1/g \ll 1$), such corrections are negligible. As the disorder becomes stronger so that $1/g > \frac{1}{3}$, the MC due to the WL are suppressed and the transport enters the WI regime. In principle, such a transport regime is also allowed in the ultrathin TI films, if the long-range disorder could be reduced to a reasonable level and the chemical potential is brought sufficiently close to the edge of hybridization gap. As depicted in Fig. 6, the dependence of α on $1/g$ in our ultrathin TI samples follows a drastically different path because of the presence of long-range disorder. Therefore, the transport in ultrathin TIs should not be regarded as a simple crossover between the WAL and the WL-WI regimes since the inhomogeneity plays an important role in the mesoscopic electronic structure.

V. CONCLUSION

We have investigated magnetotransport properties of BST thin films with thicknesses ranging from 10 to 2 nm. Positive MCs in line with the crossover to WL have not been observed despite the efforts on protecting the samples from degradation, tuning the chemical by a large range, and carrying out the transport measurements at various temperatures. We attribute the absence of global WL to the disorder-induced long-range electrostatic potential fluctuations and quantum corrections due to the second-order quantum corrections and the EEI effect. The joint influences of electronic inhomogeneity, Berry phase, quantum interference, and EEI make the magnetotransport in ultrathin TIs exhibit some unique characteristics that are distinctively different from the WAL, WL, WI, and Anderson insulator.

ACKNOWLEDGMENTS

We thank Professor H. Z. Lu for the valuable assistance on numerical calculations, and Z. C. Wang for helpful

discussions. This work was supported by the National Key Research and Development Program of China (Grants No. 2022YFA1403800 and No. 2022YFA1403403), the National Natural Science Foundation of China (Grants No.

11961141011 and No. 12274445), the Strategic Priority Research Program of Chinese Academy of Sciences (Grant No. XDB28000000), and the Youth Innovation Promotion Association of the Chinese Academy of Sciences.

-
- [1] B. L. Altshuler, D. Khmel'nitzkii, A. I. Larkin, and P. A. Lee, *Phys. Rev. B* **22**, 5142 (1980).
- [2] L. Van den dries, C. Van Haesendonck, Y. Bruynseraede, and G. Deutscher, *Phys. Rev. Lett.* **46**, 565 (1981).
- [3] G. Bergman, *Phys. Rev. Lett.* **48**, 1046 (1982).
- [4] S. Hikami, A. I. Larkin, and Y. Nagaoka, *Prog. Theor. Phys.* **63**, 707 (1980).
- [5] T. Ando, T. Nakanishi, and R. Saito, *J. Phys. Soc. Jpn.* **67**, 2857 (1998).
- [6] H. Suzuura and T. Ando, *Phys. Rev. Lett.* **89**, 266603 (2002).
- [7] K. Kechedzhi, V. I. Fal'ko, E. McCann, and B. L. Altshuler, *Phys. Rev. Lett.* **98**, 176806 (2007).
- [8] R. V. Gorbachev, F. V. Tikhonenko, A. S. Mayorov, D. W. Horsell, and A. K. Savchenko, *Phys. Rev. Lett.* **98**, 176805 (2007).
- [9] F. V. Tikhonenko, D. W. Horsell, R. V. Gorbachev, and A. K. Savchenko, *Phys. Rev. Lett.* **100**, 056802 (2008).
- [10] X. Wu, X. Li, Z. Song, C. Berger, and W. A. de Heer, *Phys. Rev. Lett.* **98**, 136801 (2007).
- [11] F. V. Tikhonenko, A. A. Kozikov, A. K. Savchenko, and R. V. Gorbachev, *Phys. Rev. Lett.* **103**, 226801 (2009).
- [12] M. Z. Hasan and C. L. Kane, *Rev. Mod. Phys.* **82**, 3045 (2010).
- [13] X.-L. Qi and S.-C. Zhang, *Phys. Today* **63**(1), 33 (2010).
- [14] Y. Xu, I. Miotkowski, and Y. P. Chen, *Nat. Commun.* **7**, 11434 (2016).
- [15] R. Yoshimi, A. Tsukazaki, Y. Kozuka, J. Falson, K. S. Takahashi, J. G. Checkelsky, N. Nagaosa, M. Kawasaki, and Y. Tokura, *Nat. Commun.* **6**, 6627 (2015).
- [16] P. Roushan, J. Seo, C. V. Parker, Y. S. Hor, D. Hsieh, D. Qian, A. Richardella, M. Z. Hasan, R. J. Cava, and A. Yazdani, *Nature (London)* **460**, 1106 (2009).
- [17] H. Z. Lu, J. Shi, and S. Q. Shen, *Phys. Rev. Lett.* **107**, 076801 (2011).
- [18] J. Chen, X. Y. He, K. H. Wu, Z. Q. Ji, L. Lu, J. R. Shi, J. H. Smet, and Y. Q. Li, *Phys. Rev. B* **83**, 241304(R) (2011).
- [19] H. Steinberg, J.-B. Laloë, V. Fatemi, J. S. Moodera, and P. Jarillo-Herrero, *Phys. Rev. B* **84**, 233101 (2011).
- [20] J. Lee, J. Park, J.-H. Lee, J. S. Kim, and H.-J. Lee, *Phys. Rev. B* **86**, 245321 (2012).
- [21] M. Brahlek, N. Koirala, M. Salehi, N. Bansal, and S. Oh, *Phys. Rev. Lett.* **113**, 026801 (2014).
- [22] J. Chen, H. J. Qin, F. Yang, J. Liu, T. Guan, F. M. Qu, G. H. Zhang, J. R. Shi, X. C. Xie, C. L. Yang, K. H. Wu, Y. Q. Li, and L. Lu, *Phys. Rev. Lett.* **105**, 176602 (2010).
- [23] Y. S. Kim, M. Brahlek, N. Bansal, E. Edrey, G. A. Kapilevich, K. Iida, M. Tanimura, Y. Horibe, S.-W. Cheong, and S. Oh, *Phys. Rev. B* **84**, 073109 (2011).
- [24] F. Xiu, L. He, Y. Wang, L. Cheng, L.-T. Chang, M. Lang, G. Huang, X. Kou, Y. Zhou, X. Jiang, Z. Chen, J. Zou, A. Shailos, and K. L. Wang, *Nat. Nanotechnol.* **6**, 216 (2011).
- [25] M. Liu, J. Zhang, C. Z. Chang, Z. Zhang, X. Feng, K. Li, K. He, L. L. Wang, X. Chen, X. Dai, Z. Fang, Q. K. Xue, X. Ma, and Y. Wang, *Phys. Rev. Lett.* **108**, 036805 (2012).
- [26] Z. Zhang, X. Feng, M. Guo, K. Li, J. Zhang, Y. Ou, Y. Feng, L. Wang, X. Chen, K. He, X. Ma, Q. Xue, and Y. Wang, *Nat. Commun.* **5**, 4915 (2014).
- [27] P. Wei, F. Katmis, B. A. Assaf, H. Steinberg, P. Jarillo-Herrero, D. Heiman, and J. S. Moodera, *Phys. Rev. Lett.* **110**, 186807 (2013).
- [28] Q. I. Yang, M. Dolev, L. Zhang, J. Zhao, A. D. Fried, E. Schemm, M. Liu, A. Palevski, A. F. Marshall, S. H. Risbud, and A. Kapitulnik, *Phys. Rev. B* **88**, 081407(R) (2013).
- [29] A. Kandala, A. Richardella, D. W. Rench, D. M. Zhang, T. C. Flanagan, and N. Samarth, *Appl. Phys. Lett.* **103**, 202409 (2013).
- [30] A. A. Taskin, S. Sasaki, K. Segawa, and Y. Ando, *Phys. Rev. Lett.* **109**, 066803 (2012).
- [31] N. Bansal, Y. S. Kim, M. Brahlek, E. Edrey, and S. Oh, *Phys. Rev. Lett.* **109**, 116804 (2012).
- [32] D. Kim, P. Syers, N. P. Butch, J. Paglione, and M. S. Fuhrer, *Nat. Commun.* **4**, 2040 (2013).
- [33] M. Lang, L. He, X. Kou, P. Upadhyaya, Y. Fan, H. Chu, Y. Jiang, J. H. Bardarson, W. Jiang, E. S. Choi, Y. Wang, N. C. Yeh, J. Moore, and K. L. Wang, *Nano Lett.* **13**, 48 (2013).
- [34] J. Liao, Y. Ou, X. Feng, S. Yang, C. Lin, W. Yang, K. Wu, K. He, X. Ma, Q.-K. Xue, and Y. Li, *Phys. Rev. Lett.* **114**, 216601 (2015).
- [35] J. Liao, G. Shi, N. Liu, and Y. Li, *Chin. Phys. B* **25**, 117201 (2016).
- [36] D. Nandi, B. Skinner, G. H. Lee, K. F. Huang, K. Shain, C.-Z. Chang, Y. Ou, S. P. Lee, J. Ward, J. S. Moodera, P. Kim, B. I. Halperin, and A. Yacoby, *Phys. Rev. B* **98**, 214203 (2018).
- [37] J. Linder, T. Yokoyama, and A. Sudbø, *Phys. Rev. B* **80**, 205401 (2009).
- [38] C.-X. Liu, H. J. Zhang, B. Yan, X.-L. Qi, T. Frauenheim, X. Dai, Z. Fang, and S.-C. Zhang, *Phys. Rev. B* **81**, 041307(R) (2010).
- [39] H.-Z. Lu, W.-Y. Shan, W. Yao, Q. Niu, and S.-Q. Shen, *Phys. Rev. B* **81**, 115407 (2010).
- [40] Y. Zhang, K. He, C.-Z. Chang, C.-L. Song, L.-L. Wang, X. Chen, J.-F. Jia, Z. Fang, X. Dai, W.-Y. Shan, S.-Q. Shen, Q. Niu, X.-L. Qi, S.-C. Zhang, X.-C. Ma, and Q.-K. Xue, *Nat. Phys.* **6**, 584 (2010).
- [41] Y. Liu, G. Bian, T. Miller, M. Bissen, and T. C. Chiang, *Phys. Rev. B* **85**, 195442 (2012).
- [42] Y. Jiang, Y. Wang, M. Chen, Z. Li, C. Song, K. He, L. Wang, X. Chen, X. Ma, and Q.-K. Xue, *Phys. Rev. Lett.* **108**, 016401 (2012).
- [43] T. Zhang, J. Ha, N. Levy, Y. Kuk, and J. Stroschio, *Phys. Rev. Lett.* **111**, 056803 (2013).

- [44] S.-Y. Xu, M. Neupane, C. Liu, D. Zhang, A. Richardella, L. Andrew Wray, N. Alidoust, M. Leandersson, T. Balasubramanian, J. Sánchez-Barriga, O. Rader, G. Landolt, B. Slomski, J. Hugo Dil, J. Osterwalder, T.-R. Chang, H.-T. Jeng, H. Lin, A. Bansil, N. Samarth, and M. Zahid Hasan, *Nat. Phys.* **8**, 616 (2012).
- [45] X. He, T. Guan, X. Wang, B. Feng, P. Cheng, L. Chen, Y. Li, and K. Wu, *Appl. Phys. Lett.* **101**, 123111 (2012).
- [46] See Supplemental Material at <http://link.aps.org/supplemental/10.1103/PhysRevB.107.115112>, which contains detailed sample characterizations, measurements, and calculations.
- [47] J. Zhang, C. Z. Chang, Z. Zhang, J. Wen, X. Feng, K. Li, M. Liu, K. He, L. Wang, X. Chen, Q. K. Xue, X. Ma, and Y. Wang, *Nat. Commun.* **2**, 574 (2011).
- [48] M. Lang, L. He, F. Xiu, X. Yu, J. Tang, Y. Wang, X. Kou, W. Jiang, A. V. Fedorov, and K. L. Wang, *ACS Nano* **6**, 295 (2012).
- [49] F. Yang, A. A. Taskin, S. Sasaki, K. Segawa, Y. Ohno, K. Matsumoto, and Y. Ando, *ACS Nano* **9**, 4050 (2015).
- [50] Y. Xu, G. Jiang, I. Miotkowski, R. R. Biswas, and Y. P. Chen, *Phys. Rev. Lett.* **123**, 207701 (2019).
- [51] D. Kong, Y. Chen, J. J. Cha, Q. Zhang, J. G. Analytis, K. Lai, Z. Liu, S. S. Hong, K. J. Koski, S. K. Mo, Z. Hussain, I. R. Fisher, Z. X. Shen, and Y. Cui, *Nat. Nanotechnol.* **6**, 705 (2011).
- [52] B. Skinner, T. Chen, and B. I. Shklovskii, *Phys. Rev. Lett.* **109**, 176801 (2012).
- [53] H. Beidenkopf, P. Roushan, J. Seo, L. Gorman, I. Drozdov, Y. S. Hor, R. J. Cava, and A. Yazdani, *Nat. Phys.* **7**, 939 (2011).
- [54] D. Culcer, A. Cem Keser, Y. Li, and G. Tkachov, *2D Mater.* **7**, 022007 (2020).
- [55] The only exception was reported in Ref. [33], in which 4-QL and 5-QL BST films exhibit slightly positive MC in low magnetic fields. However, it is noteworthy that an ARPES experiment showed that the surface states of 5-QL BST films remain gapless for any Bi/Sb composition ratio [47]. One likely scenario is the actual thicknesses of the BST films are smaller than the nominal values. It would be interesting if similar positive MC could be observed in future studies.
- [56] B. Skinner, T. Chen, and B. I. Shklovskii, *J. Exp. Theor. Phys.* **117**, 579 (2013).
- [57] C. Kastl, P. Seifert, X. He, K. Wu, Y. Li, and A. Holleitner, *2D Mater.* **2**, 024012 (2015).
- [58] G. Shi, F. Gao, Z. Li, R. Zhang, I. Gornyi, D. Gutman, and Y. Li, [arXiv:2210.12973](https://arxiv.org/abs/2210.12973).
- [59] G. M. Minkov, A. V. Germanenko, and I. V. Gornyi, *Phys. Rev. B* **70**, 245423 (2004).
- [60] B. T. Schaefer, L. Wang, A. Jarjour, K. Watanabe, T. Taniguchi, P. L. McEuen, and K. C. Nowack, *Nat. Commun.* **11**, 4163 (2020).